Title

In situ transmission electron microscopy investigation of electroplasticity in single crystal nickel

Authors

Li, Xiaoqing
Turner, John
Bustillo, Karen
et al.

Publication Date

2022

DOI

10.1016/j.actamat.2021.117461

Acta Materialia 223 (2022) 117461

Contents lists available at ScienceDirect

Acta Materialia

journal homepage: www.elsevier.com/locate/actamat

In situ transmission electron microscopy investigation of electroplasticity in single crystal nickel

Xiaoqing Li[a,b], John Turner[b], Karen Bustillo[b], Andrew M. Minor[a,b,*]

[a] University of California Berkeley, Department of Materials Sciences and Engineering, Berkeley, USA
[b] National Center for Electron Microscopy, Molecular Foundry, Lawrence Berkeley National Laboratory, Berkeley, CA, USA

ARTICLE INFO

Article history:
Received 1 July 2021
Revised 2 October 2021
Accepted 1 November 2021
Available online 4 November 2021

Keywords:
in situ TEM
Nanomechanical test
Electroplasticity
Primary dislocation
Slip band
Surface dislocation nucleation

ABSTRACT

In situ Transmission Electron Microscopy (*in situ* TEM) tensile tests of single crystal nickel were performed in order to correlate direct observations of nanostructural changes resulting from applied mechanical and electrical stimuli in an effort to provide clarity on the mechanisms of electroplasticity (EP). A dual-tensile geometry was tested with an electrical push-to-pull device (EPTP) and digital image correlation (DIC) was used to track the location of dislocation nucleation along the sample surface. By analyzing the change in sample geometry precisely we are able to directly track individual dislocation motion as a result of the combined electromechanical actuation. From our observations, the pulsed electrical current leads to a more uniform deformation as compared to purely mechanically triggered plasticity. When the sample is undergoing stable plastic deformation, the pulsed current delays the formation of a stress concentration and distributes the deformation more uniformly. Our analysis finds that enhancement of surface nucleation from the electron wind force is more likely than Joule heating to be the origin of the more uniform plasticity observed during electrical pulsing.

1. Introduction

Electroplasticity (EP) is a phenomenon in which applied pulsed electric fields during plastic deformation result in a reduction in flow stress and increased strain prior to failure [1]. Starting in the 1960s [2], scientists used this phenomenon as an alternative forming method at relatively low temperature called "electrically-assisted forming". EP technologies include either constant or pulsed electrical currents then been used to improve the formability of high strength, brittle, and difficult-to-form engineering metals [3]. The ductility enhancements resulting from EP are often considered separate from thermal-mechanical behavior and are thought to be related to alternative electronic effects on dislocations [4] because the measured temperatures are deemed lower than those necessary to induce similar levels of thermal softening [5]. Recent work has shown that dislocation morphology can be changed with electrical pulsing in a manner that cannot be directly attributed to simple Joule heating [6]. However, direct defect-level observations are required to clarify the influence of the various mechanisms, which we intend to further with the results presented here.

A recent publication studied the dislocation evolution of a Ni-based superalloy (Inconel 718) with an applied electrical current by *in situ* Transmission Electron Microscopy (*in situ* TEM) and directly compared to an *in situ* TEM heating experiment [7]. The researchers found the dislocations annihilate at first and then regenerate with electrical current, in contrast to only annihilating in the heating experiment. Calculations were also done in this study on evaluating many different effects [7]. They found the direct effect of drift electrons on the dislocation motion contributes primarily to the plastic strain, instead of side effects such as skin, pinch, instantaneous thermal expansion stress, and Joule heating. The EP effect was also observed in *in situ* mechanical tests trying to understand the electrical current pulsing methods [8].

Although there have been bulk tests with temperature tracking and *ex situ* / *in situ* material structural analysis trying to study the microstructures change [9], it has not been possible to examine plastic deformation at the defect level with *in situ* TEM, (either single dislocation dynamics or single slip band formation changing with the applied external electrical current). Recent advances *in situ* TEM testing methodologies have demonstrated increasingly stable mechanical loading [10,11]. In particular, *in situ* tensile test-

* Corresonding author.
E-mail address: aminor@lbl.gov (A.M. Minor).

https://doi.org/10.1016/j.actamat.2021.117461

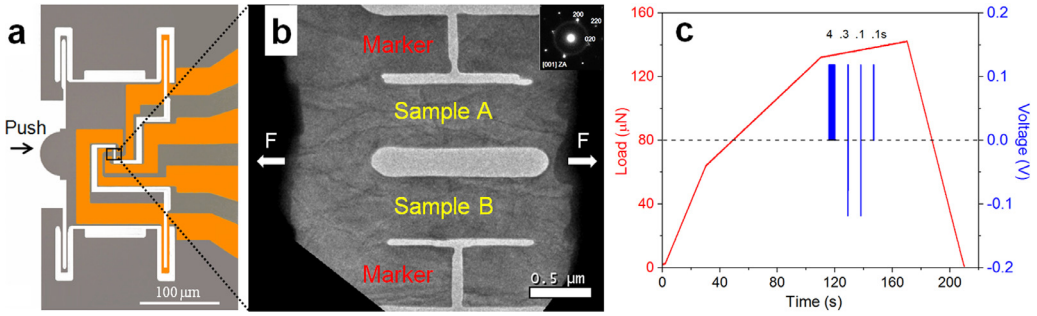

Fig. 1. Experimental configuration and controlled parameters. (a) EPTP device, gold patterns are conductive electrodes for electrical current measurements. (b) Sample geometry during *in situ* mechanical tests, the two continuous pieces in the middle are samples A and B, respectively, and two gaps on both sides are the "markers". (c) A typical loading curve, with load control *vs* time and the electrical current supplied with a voltage control *vs* time.

ing with the 'push-to-pull' device (PTP), a type of micro-electro-mechanical systems (MEMSs) device, enables stable tensile testing of thin films and nanowires inside a TEM. With this technique, dislocation motion can be directly observed, and many small-scale plasticity mechanisms were studied [12,13]. For example, intrinsic dislocation mechanisms were studied in a nearly pristine single crystal Ni sample prepared by focused-ion-beam (FIB) [14], and found that plasticity was mostly controlled by the preexisting dislocations acting as a single arm source. Lately, a study from our group also used this technique to measure the activation volume of dislocation nucleation [15]. Electrical push-to-pull devices (EPTP) have been used to apply controlled electrical and mechanical stimuli to the samples to study their properties during *in situ* TEM experiments. For example, this device was used to study the piezoresistive response of quasi-one-dimensional ZnO nanowires [16]. The device enabled the application of tensile strain and measurement of *in situ* electrical properties simultaneously. More recently, individual InAs core-shell nanowires were studied with EPTP and the results provide a direct correlation of nanoscale mechanical strain and electrical transport properties [17].

In our study, the EPTP platform was used to perform *in situ* TEM electromechanical tests on a pure single crystal Ni foil. Our experiments were designed in order to correlate direct observations of dislocation motion with both mechanical deformation and applied electrical pulses in an effort to provide clarity on the mechanisms of electroplasticity. With the special design of sample geometry and digital image correlation (DIC) technique, we were able to obtain the distribution of nucleated primary dislocation along the sample surface. With the formation of slip bands on the sample, we found the electrical current leads to more uniform deformation and reduces stress localization. Lastly, surface dislocation nucleation theory and the effect of electrical current is discussed to explain the observed slip band development.

2. Methodology

2.1. Sample preparation

As-received 99.994% pure Ni foil (Puratronic) with a thickness of 0.1 mm was annealed in a furnace at 700 °C for 1 hour. 3 mm disks were punched out of the foil and conventional twin-jet electropolishing was performed with a solution of 6% perchloric acid, 55% methanol and 39% ethanol, at 10 V and −25 °C. In order to optimize the *in situ* TEM loading conditions, electron back-scattered diffraction (EBSD) was used to identify the orientation of selected grains. Grains with the ⟨001⟩ zone axis were then selected for the fabrication of the samples to precisely orient the specimen for loading. Dual-beam FIB techniques were used to create the special dual-tensile design as shown in Fig. 1. To remove as much surface damage as possible from the samples, a JEOL 3010 TEM was used for in-vacuum annealing. The annealing conditions for Ni was 400 °C for 7mins followed by 700 °C for 3 mins. Diffraction patterns (DPs) were obtained to check the sample orientation and **g** dot **b** analysis was performed to characterize the preexisted dislocations for the eventual *in situ* TEM experiments. TEM energy dispersive X-ray analysis (EDX) showed there was an oxide layer on the surface after annealing, but the Ga^+ ion damage seemed reduced and the transparency of the sample was improved, and more details can be found in Supplementary Materials.

2.2. EPTP devices and sample geometry

The experiment setup utilizing an EPTP with gold electrodes for electrical contacts is shown in Fig. 1(a), and a detailed description of the EPTP can be found in the Supplementary Materials Fig. S1. An electron-transparent metal film (10 μm × 3 μm) was lifted out from a 3 mm jet polished sample in a Focused Ion Beam (FIB) and placed across the gap of the EPTP. The section hanging above the gap was further shaped to a modified dog-bone with the FIB. Two milled slits, "markers", on both sides of the sample were made. They were used for measuring the precise elongation of the dog-bone area of the sample with a spatial resolution of sub-nanometer, as shown in Fig. 1(b). The aligned specimen attached to the EPTP device was deformed uniaxially in tension to correlate the dislocation behavior, applied mechanical loading, and electrical current with respect to each other in time.

In situ mechanical testing was carried out in a JEOL 3010 TEM using a Hysitron, Inc. picoindentater. The system combined with the EPTP can generate reproducible load-displacement curves during plastic deformation via load control. The data acquisition rate for load-displacement measurement is 200 points/*sec*. An example of a dual mechanical loading and voltage-controlled experiment programmed as a function of time is shown in Fig. 1(c). In this experiment, an applied voltage with a maximum value of 0.12 V, which is equivalent to a current density of $J = 1.25 \times 10^4 \mathrm{A/mm^2}$, was applied to the sample. A specific pattern of applied electrical current is performed for each test: 4 s of constant current at 116 s, two current sweeps of 0.3 s at 129 second, 0.1 s at 138 s and another constant current of 0.1 s at 147 s. A more detailed description of the pattern of the applied electrical voltage can be found in the Supplementary Fig. S3 and Table S1.

For each test, the load, displacement, voltage, current and videos of the dog-bone area were recorded. Contrast changes in the specimen and the elongation of the sample were analyzed frame by frame and colorized to indicate spatially where the sample had changed. Details of this method can be found in our previous publication [15]. With a frame rate of 24 frames per second, it is not possible to observe single defect motion, but contrast changes and shape changes in the specimen due to defect motion is observable. The elongation of the dog-bone is measured directly via the

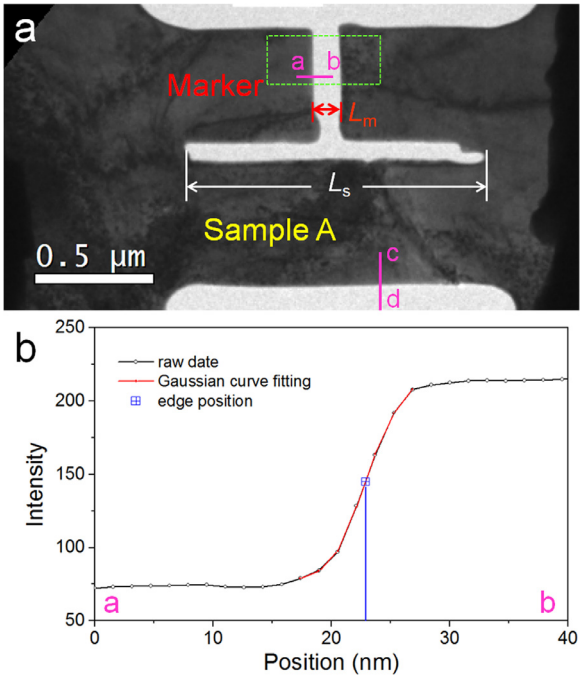

Fig. 2. Precise measurement of edge position by contrast analysis of bright field (BF) image. (a) BF images of the sample. Measurements were taken from point a to point b for tracing the position of the "markers", and point c to point d for tracing the edge profile. L_s indicates the sample length, and L_m is the length of marker. The green box indicates the "marker" area used for elongation measurement. (b) An example brightness intensity profile from point a to point b across the edge of the marker. Gaussian curve fitting and the FWHM used to determine the precise position of edge.

elongation of the "marker", which is determined by averaging the change in distance between the two sides of the marker for each frame in the green box, as shown in Fig. 2(a). In each bright field (BF) diffraction contrast image, a brightness intensity profile was used to determine the edge of the sample. For example, "point a to point b" for tracing the position of "markers", and "point c to point d" for tracing the edge profile. A Gaussian curve fitting was performed for each intensity curve, and the position for the full-width-half-max (FWHM) of the fitted line was determined to be the "precise edge position" at the sharpest contrast change, as shown in Fig. 2(b). By calculating the derivative of the fitted line, the accuracy of measurement is improved to 0.2 nm, corresponding to a 1.58 nm pixel resolution from the original BF image. By tracing off the precise position of the edges on the sample, the plastic deformation of the sample and dislocation movement can be matched with the precise elongation measurement of the dog-bone. Moreover, the measured elongation changes of the dog-bone area are indirect indicators of plasticity with dislocation motions and can be time-correlated with the electrical current data. More specifically, direct measurement of the local deformation can be recorded from changes in the edge profile analysis in the lateral direction on the scale of a single dislocation, with a schematic shown in Fig. 3. The edge profile analysis results in a better representation of the position of a slip band, which will be discussed in the result section.

2.3. Sample orientation

The specific sample geometry consisted of two dog-bone shaped pieces each with a dimension of 1200 nm in length, 500 nm in width and roughly 80 nm in thickness. The specimen was fabricated with a viewing orientation perpendicular to the electron beam such that it was close to a ⟨001⟩ zone and had a

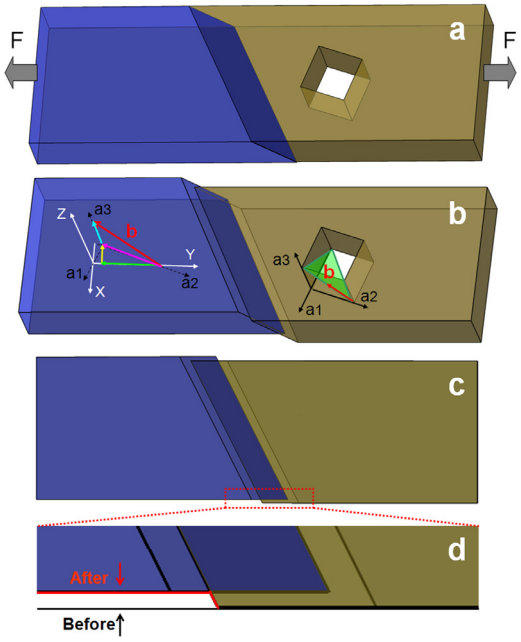

Fig. 3. Schematic representation of the sample geometry and crystallographic orientation. (a) 3D view of initial dog-bone shaped sample without deformation. The $(\bar{1}11)$ plane is shown in shaded. (b) 3D view of the sample with a ledge following the slip plane, with a ⟨001⟩ zone and had a loading direction of $[\bar{1}30]$. (c) Top view of the sample after slip band formation. (d) Two schematic edge profiles corresponding to before and after the dislocation slip formation are marked in the red dotted box in (c). The red lines trace out the shape of the sample edge profile.

Table 1
Schmid factor analysis of possible primary slip systems.

Planes	Directions	Schmid Factor
111	$0\bar{1}1$	−0.2449
111	$\bar{1}10$	0.3266
111	$10\bar{1}$	−0.0816
$\bar{1}11$	101	−0.1633
$\bar{1}$11	**$0\bar{1}1$**	**−0.4899**
$\bar{1}11$	110	0.3266
$11\bar{1}$	101	−0.0816
$11\bar{1}$	011	0.2449
$11\bar{1}$	$\bar{1}10$	0.3266
$1\bar{1}1$	$\bar{1}01$	−0.1633
1$\bar{1}$1	**011**	**−0.4899**
$1\bar{1}1$	110	−0.3266

loading direction of roughly $[\bar{1}30]$. A schematic image showing the crystal orientation in Fig. 3(a), the crystallographic coordinate system is marked by ($\mathbf{a_1}$, $\mathbf{a_2}$, $\mathbf{a_3}$), and the tensile coordinate system of the sample is shown by (**X, Y, Z**), with the perpendicular **X** (width), the tensile **Y** (length), and the thickness **Z** directions, in Fig. 3(b).

For FCC Ni single crystal oriented in the $[\bar{1}30]$ loading direction, the predominant slip activity can be observed in ⟨001⟩ viewing direction [18]. Specifically, calculation of the resolved shear stress (RSS) for this orientation predicts that the primary slip system to be activated would be the $(\bar{1}11)$ slip plane in the $[0\bar{1}1]$ direction, as shown in Table 1. An equivalent slip direction is on $(1\bar{1}1)$ slip plane in [011] direction and a schematic representation of the two systems is shown in Supplementary Materials Fig. S2. Based on the sample geometry and orientation analysis, primary dislocations can glide through the sample from one edge to the other edge as shown schematically by the slipped plane in Fig. 3(b).

To analyze the three-dimensional geometric change of the sample due to the movement of a single dislocation gliding through, the Burger's vector **b** was projected onto three directions of the

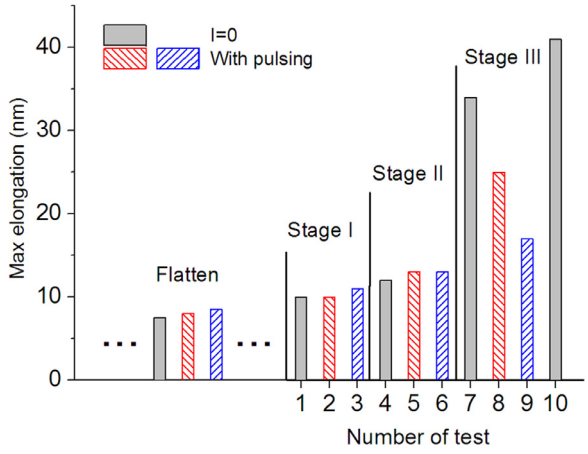

Fig. 4. Summary of the elongations for 10 sequential tests on the same sample before fracture. Each bar represented the maximum change of elongation of sample during that test. The black filled bars are the tests with only mechanical actuation. The red and blue color were used to distinguish the two sets of tests, but both marked the tests with applied electrical current and mechanical actuation.

sample as shown in Fig. 3(c). Burger's vector **b** is drawn in red arrow with $\boldsymbol{b} = a/2[0\bar{1}1]$, where $a = 0.353$ nm is the lattice parameter of nickel. Theoretically, for a primary dislocation gliding on the $(\bar{1}11)$ plane in the $[0\bar{1}1]$ direction, after traveling across the whole sample, the measured elongation from before to after a slip event in the length direction is $dY = 0.167$ nm. The ratio of the distance change by the slipped ledge projected in the tensile direction and the perpendicular direction is 3:1, which leads to an edge profile measurement that can be calculated as $dX = dY/3 = 0.0558$ nm. Detailed calculation is shown in Supplementary Materials. As a result of this single crystal geometry, we can quantitatively relate the change of the edge profile for the inner side of the samples, as shown by the schematic in Fig. 3(d) with the numbers of dislocations gliding on this specific plane.

3. Results

3.1. Description of the experiment

In the experiment, a sequence of alternating tests was performed on a single crystal nickel specimen with one test of pure mechanical loading and two tests with electrical current, following the pulse pattern shown in Fig. 1(c). After each elongation the device was relaxed and then loaded again. The electrical current was applied alternatively to these tests to create comparable conditions on the same sample for each series of tests, with the full details for applied electrical current with time described in the Supplementary Materials Fig. S3. This scheme was selected to emphasize the electrical current tests while still maintaining a substantial amount of plasticity for comparison. With this method, we could produce a series of repeated experiments that are comparable to each other such that there is active plasticity induced by the mechanical deformation before, during and after the electrical pulses. At the beginning of the test sequence, the sample was first undergoing a flattening process where little to no plasticity was evident, as shown in Fig. 4. During this process, the sample did not undergo noticeable plasticity in the gage section but was primarily straightened flat from any slight bending inherent in the sample or incurred during the manipulation and placement on the EPTP device. After the flattening process, the EPTP was pulled taut and the dog-bone area began to bear load. In this work, we presented the analysis of a test specimen that was partitioned into two samples (A and B) and subjected to 10 consecutive and separate tests. The plastic deformation process was further described with three stages (Stage I, II and III) as summarized in Fig. 4. The markers on the sample were considered to give a more stable and precise measurement of the real elongation of the dog-bone area in each test.

The plastic deformation process was divided into three stages according to the elongation curves and the type of plastic deformation mechanisms that were activated. During stage I, local plastic deformation was observed that consisted of elimination and annihilation of existing dislocations. This phenomenon is sometimes described as "mechanical annealing" [19], where preexisting defects are eliminated upon early loading in nanoscale *in situ* tests in samples that have extensive surface area to serve as sinks. Most of the deformation in this process was localized, with small elongation jumps (< 0.2 nm), and observed by permanent changes in contrast, shown in Fig. 5(a, c). Since the annihilation of preexisting dislocations only resulted in a small adjustment locally, it was not possible to see any change via the elongation measurements of the markers. During stage II large areas on the dog-bone started to show a clear measurable plasticity that was easily observed on the elongation curves. The start of stage II was distinguished by many dislocations nucleating in bursts from the surface of the sample causing a clear 0.2~4 nm jump in 0.2 s, shown on the elongation curves in Fig. 5(b). These dislocations were consistent with primary dislocations nucleating from the surface of the sample and gliding in the direction of maximum RSS. As shown in Fig. 5(b, d), large areas of contrast change exhibit relatively continuous stable plasticity during stage II.

3.2. Slip band formation and development in stage III

In stage III (tests 7 to 10), the plastic deformation resulted in slip band formation and progression. As shown in Fig. 6, a slip band was apparent after nucleation of many dislocations from the surface of the sample that then slipped in one event (within the timeframe of the experiment) following the maximum RSS and left a clear geometric change as observed on the edge of the sample. The formation of the slip band is in agreement with the theoretical analysis of the sample crystallographic orientation and tension direction in Fig. 3. Finally, the failure occurred at the weakest area on the sample at the slip bands in Fig. 6(d2).

As shown in Fig. 6(a, b1–2), there was an 18 nm jump on the elongation curve in test 7 that corresponded to the slip band formation in sample A. During test 8, a 5.5 nm jump occurred at the start of an electrical current pulse, corresponding to a further extension of the slip band on sample A as shown in Fig. 6(a, c1–2). In test 9, the whole specimen deformed uniformly, and no sudden jump was observed on the elongation curve. In test 10, a pure mechanical test, sample B formed a slip band following the same slip trace of the slip band on sample A, and the elongation measurement showed a 14 nm jump. Four seconds after the slip band formed on sample B, the sample fractured at the location of the slip bands on sample A and B, as shown in Fig. 6(a, d1–2). A more detailed analysis of the fracture is discussed in the Supplementary Materials Fig. S4. Interestingly, the formation of the slip bands in both sample A and B happened during purely mechanical tension, in test 7 and 10, respectively. In test 8, the slip band on sample A only extended slightly when an electrical current was applied. A supplementary video of the slip band formation and development can be found in the Supplementary Materials.

3.3. Change of edge profile as a measure of the spatial distribution of plasticity

Because of the single crystal geometry of the sample, it is possible to directly relate the change of sample edge profile to the dis-

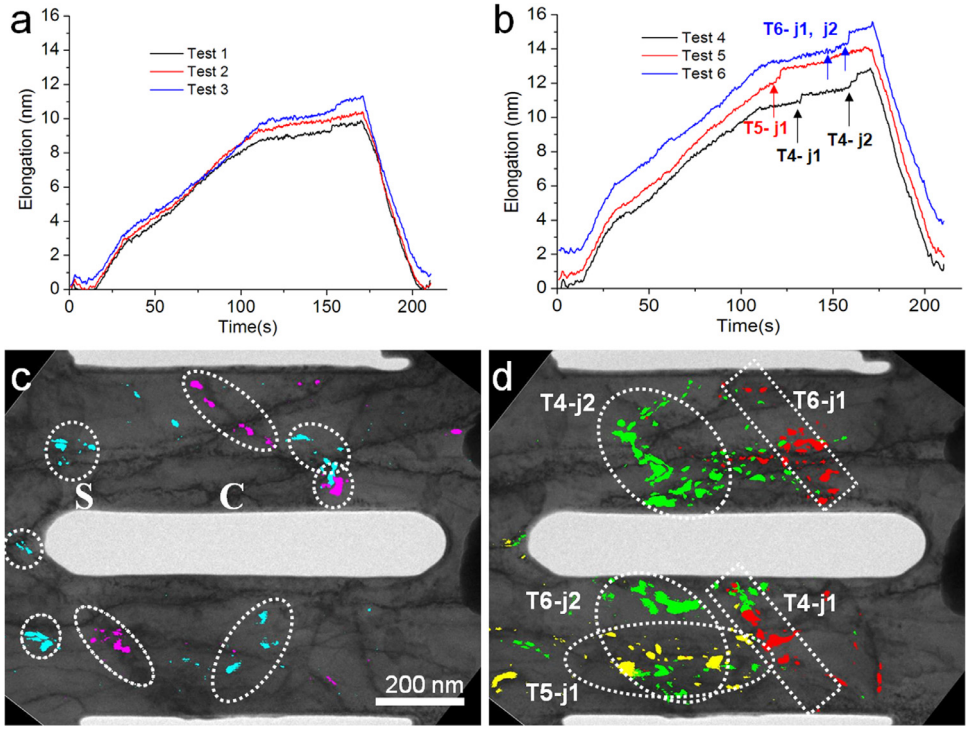

Fig. 5. Examples of deformation stage I and stage II. Elongation curves and selected frames showing the typical plastic deformation patterns in (a) stage I (tests 1 to 3) and (b) stage II (tests 4 to 6), respectively. (c-d) Changes in contrast between frames are colorized for comparison. (c) Small preexisted dislocation moved to the surface and annihilated, local deformations were dominated during stage I, progressed from shoulder (S) to the center (C) of the dog-bone area. (d) Primary dislocations nucleated from the edge and slipped through the width direction of the sample and a small group dislocation burst in large deformation area, matching the jumps in the elongation curves during stage II.

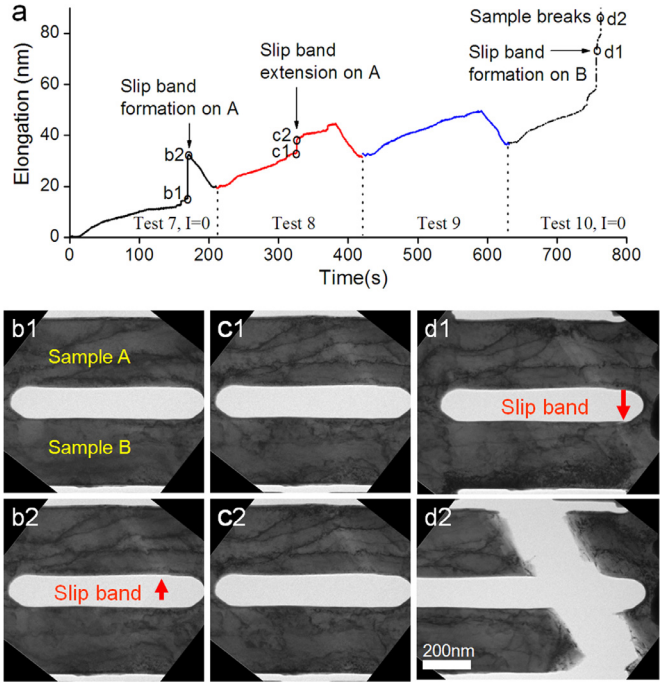

Fig. 6. Slip band formation and extension in tests 7 to 10. (a) Elongation curve with the labeled points (b1-d2) correspond to frames showing deformation before and after each big jump in elongation. (b1-b2, c1-c2, d1-d2) Corresponding frames showing slip band development and sample fracture.

tribution of plasticity along the sample during deformation. Due to the length of the profile and lower noise level, the inner side of the profiles for sample A and B were used to extract information on dislocation nucleation in the analysis that follows. For example, the change of the edge profiles for samples A at the inner surface was measured using the frames before and after the 18 nm elongation jumps in test 7, as an example shown in Fig. 7. The edge profiles were obtained by tracing out the precise edge position of the sample along each side in the frames in Fig. 7(a, b), using the image analysis technique introduced in Fig. 2. The red dotted lines mark the slip band, an area of thinning and the local stress concentration caused by a dislocation burst in sample A. The change of edge profile for the inner side of sample A is obtained by subtracting the edge profile of the after frame (red curve) from that of the before frame (black curve), and the result is shown in Fig. 7(c). The red dotted line in Fig. 7(a) marks the slip band formed in sample A, which represents a clear permanent shape change of the sample with reduced thickness and surface steps on both sides. From the edge profiles, the change in dimension perpendicular to the tensile direction for the inside surface was roughly 6 nm, corresponding to an 18 nm change in the tensile direction. In the same two frames, sample B has not developed a slip band yet, but it showed a clear band of reduced thickness and therefore stress concentration due to the dislocation burst.

The change of the edge profiles for samples A and B was measured by comparing the same two sets of frames during the slip band formation in test 7 and slip band extension in test 8 on sample A. Details of the resulted edge profile for each test and each sample can be found in Supplementary Materials Fig. S5 and Fig. S6. In Fig. 8(a), the measurement on sample A during test 7 (purely mechanical) showed a significantly larger difference, which corresponded to the slip band formation. While in test 8 (with electrical current), it showed less change for the slip band development at the same position. In Fig. 8(b), sample B was still in the stable plasticity region in both test 7 and 8, because there was no significant geometric change of the surface that indicating any slip band formation during each test. Although sample B had a small sur-

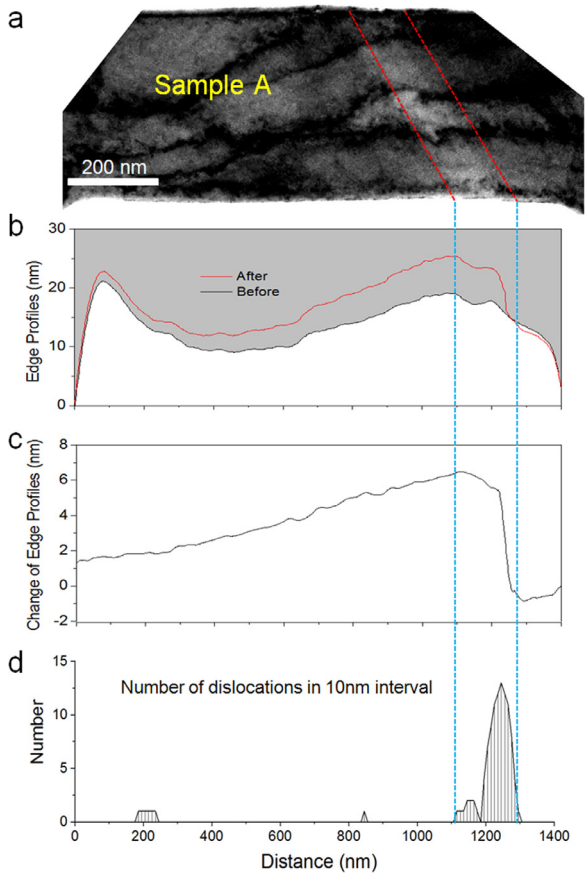

Fig. 7. Precise measurement of the edge profile. Profiles of the inner side for the sample A in test 7, corresponding to the frames in Fig. 6 (b1-b2). The gray shaded side corresponds to the sample side. (a) TEM image of sample A, the red dotted lines mark the slip band. (b) The edge profile of the inner side of sample A before (black curve) and after (red curve) the slip band formation. (c) The change of edge profile for the inner side of sample A, by subtracting the edge profile of the after frame (red curve) from that of the before frame (black curve) in (b). (d) Equivalent number of dislocations nucleated along the edges. The horizontal axises of the plots share the same scale, labeled as distance, and matched with the length of the corresponding edges in the image.

face disruption caused by a dislocation burst in test 7, any change in the edge profile on sample B in test 8 was not obvious. In this comparison, it can be concluded that in purely mechanical tests the sample was more susceptible to slip band formation. In addition, the applied electrical pulsing appeared to be able to reduce the slip band development.

3.4. Uniformity of plasticity during electrical pulsing

The distribution of dislocation activity as a function of electrical pulsing in the samples was determined using the edge profile change of the inner edge of sample A and B. Details of the data processing techniques for dislocation analysis from the edge profile is discussed in the Supplementary Materials Fig. S7. Based on the analysis of sample crystallographic orientation and tensile direction, the calculation of RSS shows that the lateral change in the width caused by each dislocation motion is 0.056 nm. We set each interval along the sample edge in the tensile direction to be 10 nm and counted the number of nucleated dislocations by using the measured edge profile change in each interval divided by 0.056 nm. An example of calculated equivalent number of dislocations nucleated along the inner edge of sample A in shown in Fig. 7(d). All the results from this analysis of samples A and B during stage III (tests 7 to 10) are displayed in Fig. 9.

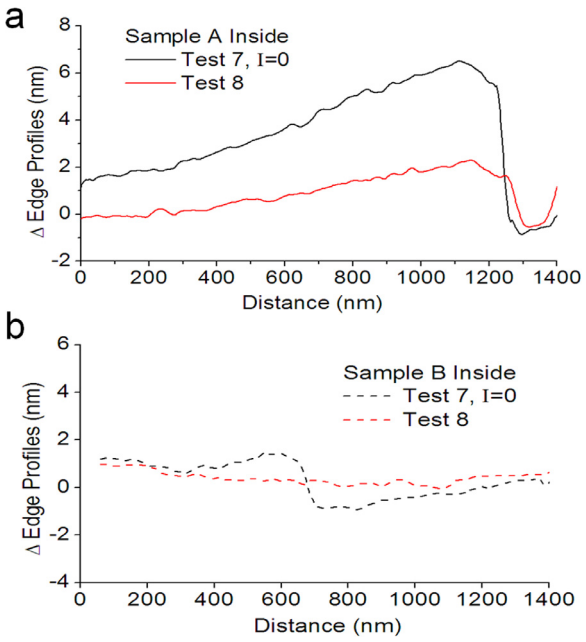

Fig. 8. Comparison of the change of edge profiles for the inner sides. (a) Sample A undergoing a purely mechanical test 7 (black line) and the electromechanical test 8 (red line). (b) Sample B in the purely mechanical test 7 (black dotted line) and the electromechanical test 8 (red dotted line).

For sample A, nearly all the dislocations were nucleated at the position of the slip band during all three tests, as shown in Fig. 9(a). Since the sample had already undergone an event leading to the geometrically thinned area, the applied stress was higher in this region and this is unsurprising. However, the situation for sample B was different. During test 7, with pure mechanical loading, sample B also developed a thinned area, but had no significant geometric surface change or slip band. As shown in Fig. 9(b), most dislocations were nucleated at the location of 600 nm, with other small amounts along the rest of the sample. During test 8, with an applied electrical current, there were still dislocation nucleation events, but they were clearly randomized along the sample, instead of being concentrated at the previously localized position of 600 nm in test 7. Test 9, a following test with applied electrical current, showed no detective elongation jumps. Test 10 was again purely mechanical and there was severe stress localization and eventually fracture at the location of the slip band.

4. Discussion

In our experiment, when the slip band formed in test 7, the sudden elongation jump was measured to be 18 nm, indicating that roughly 108 dislocation bursts happened in 0.2 s, which can be considered a dislocation avalanche leading to slip band formation. In small-volume pristine crystalline solids dislocation nucleation is likely to be the most essential deformation mechanism for plasticity [20]. The details about the energy description of single dislocation nucleation theory can be found in the Supplementary Materials.

4.1. Joule heating effect and uniform temperature rises

It is important to first consider the Joule heating effect, which we can do with an indirect measurement of the increase in temperature due to the electrical current in our experiments. From the frame-by-frame video, the instant sample elongation can be measured when an electrical current is applied. In our experiment, the

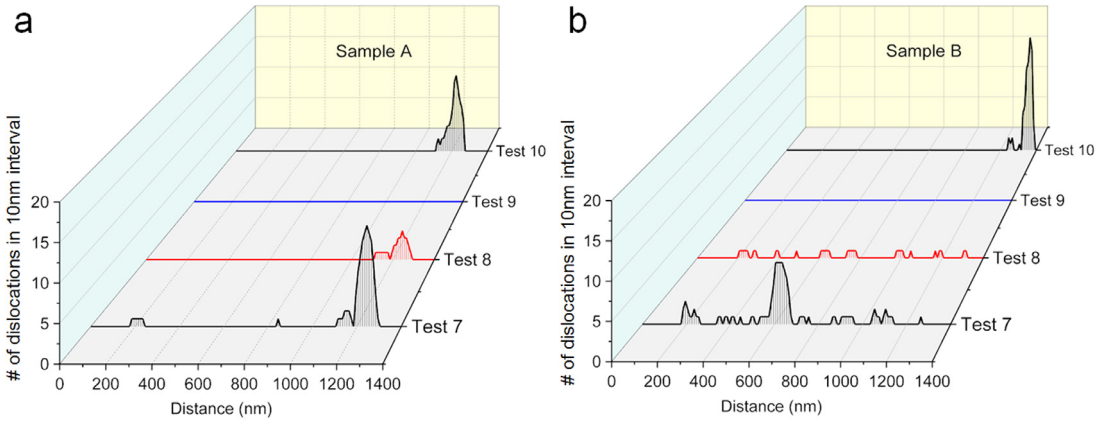

Fig. 9. Distribution of nucleated dislocations. The nucleation of dislocations counted during pure mechanical (tests 7 & 10) and the tests with electrical current (tests 8 & 9). (a) Sample A: slip band formed around 1200 nm in test 7, extended in test 8, stabilized in test 9 and fractured in test 10 at the same place. (b) Sample B: developed a stress concentrated area during test 7 at around 600 nm, experienced uniform deformation in test 8 and fractured near the shoulder in test 10.

applied current during pulsing was $J = 1.25 \times 10^4 A/mm^2$ passing through a sample with a cross-section area of 0.08 μm^2 and length of 1.2 μm. Since the minimum sample elongation that can be measured is 0.2 nm, we can assume the elongation of the sample is no more than 0.2 nm. From the linear thermal expansion coefficient of nickel $\alpha_{Ni} = 13.1 \times 10^{-6}$ (m/m °C) [21]. The temperature increase caused by Joule heating due to the applied electrical current on this sample is less than 12.72 °C. In addition, we performed calculations to confirm the uniformity of the temperature profile over the entire sample after electrical pulsing. The resistive heating generated by electrical current and the thermal conduction were taken into consideration in this model, without thermal convection and radiation. The boundary condition for the specimen was set to be a constant room temperature at the two ends, which is directly connected to heat sinks (the Au electrodes). After reaching steady-state conditions, the Poisson equation [22] predicts that the maximum temperature ΔT_{max} for a given current density J occurs at the center of the sample, and the maximum difference of temperature along the sample is given by [23]:

$$\Delta T_{max} = J^2 l^2 \frac{\rho}{8\kappa}, \quad (1)$$

where ρ is the resistivity and κ is the thermal conductivity of the specimen. Since the maximum temperature is proportional to l^2 for a given current density, the maximum temperature difference decreases rapidly with decreasing size of the specimen [24]. From the calculation with the parameters for nickel, Eq. (1) predicts that ΔT_{max} =0.02 °C at $J = 1.25 \times 10^4 A/mm^2$ for a nickel specimen of 1.2 μm length where $\rho_{Ni} = 6.4 \times 10^{-8}$ Ωm and $\kappa_{Ni} = 90$ W/(mK) [21,25]. Any heating from the electron beam can be considered to be a negligible effect, because the beam current density is approximately 6 orders of magnitude smaller than that was applied during the test and estimated to lead to a temperature change less than ΔT=0.01 K at the current density used during imaging [26]. Therefore, our analytical results predict mostly uniform and negligible temperature increases by Joule heating in a nano-scale specimen due to effective thermal energy dissipation by conduction of the generated heat to the heat sinks (gold electrodes, Si frame and TEM holder).

4.2. Wind force and its role in nucleation of dislocations from the surface

The force induced by an applied electric field on a lattice atom consists of two components: a direct force and a wind force [27]. The direct force is caused by a net charge of the migrating atom, while the wind force is caused by scattering of the current-carrying electrons from the atom. Both forces are proportional to the electric field E and to a valence Z as shown by

$$F = (Z_{direct} + Z_{wind})eE = Z^* eE. \quad (2)$$

where e is the charge of an electron, and the effective valence Z^* values for many metals were quantitatively calculated by previous studies [27].

Early experiments using scanning tunneling microscopy (STM) to observe the evolution of monolayer islands was conducted on the surface of polycrystalline gold films by atomic self-diffusion and electromigration [28]. The current densities driven through the films were in the range of 10^3 A/mm^2 to 2×10^4 A/mm^2. The results showed that with an applied current, a surface morphological change could occur in the opposite direction of the self-diffusion process. New types of surface evolution and rearrangements due to atomic diffusion were also observed, indicating a change of activation energies for atom detachment on the surface due to the applied current. More recently, similar atomically resolved structural fluctuations on a silver thin film surface under a large applied current of 10^7 A/mm^2 by STM imaging were directly correlated with the wind force mechanism. Due to this large current density, the magnitude of the momentum transfer from electrons to the atoms is ten times larger as compared to freely diffusing adatoms [29].

The combination of theoretical and experimental studies described above found that the applied electrical current can affect surface diffusion process by altering the atom movement on the surface or changing the local activation energy required for dislocation nucleation. Thus, the electropulsing effectively accelerated the movement of dislocations, which significantly improved the plasticity of the alloy and homogenized the distribution of dislocations [30]. During our experiment, there was no significant temperature increases, less than 12.72 °C, indicating a negligible Joule heating effect. However, we did observe an increase in nucleation events (more random and well distributed plasticity) during electrical pulsing than without. As our samples are operating in a nucleation-limited regime, one possible explanation for the more continuous plasticity we found during EP is therefore due to the enhanced surface diffusion resulting from the electron wind force and its potential impact on dislocation nucleation from the surfaces. A detailed analysis for the behaviors of the two samples is discussed in the Supplementary Materials Fig. S8.

5. Conclusion

In this study we conducted *in situ* TEM tensile testing of a single crystal nickel using a novel sample geometry to observe the effects of electrical current on the plastic deformation. During plastic deformation, we found that an applied electrical current led to a more uniform deformation. Even when there was a local stress intensity, the electrical current facilitated a continuously uniform deformation along the entire sample, which reduced the concentration of the local stress, though the electrical current was found to have a minor effect compared to the applied mechanical force. An analysis of the most likely origin of the more distributed plasticity found that the enhanced surface nucleation resulting from the electron wind force was likely more significant than Joule heating during electrical pulsing.

Ultimately, we demonstrated a method to study combined electromechanical effects in small samples using a truly multimodal characterization approach. By collecting multiple signals simultaneously and using the sample geometry to provide accurate measurement of surface features, we could directly correlate individual slip events with mechanical and/or electrical stimuli. By comparing and contrasting the plasticity with and without electrical current during *in situ* TEM experiments, we hope to advance the fundamental understanding of electroplasticity, and establish the foundations for incorporating electroplasticity into industrial processing of materials. Hopefully, our experimental framework provides a scientific foundation for the design and optimization of alloys with enhanced electroformability for targeted manufacturing applications.

Declaration of Competing Interest

The authors declare that they have no known competing financial interests or personal relationships that could have appeared to influence the work reported in this paper.

Acknowledgment

The authors gratefully acknowledge funding from the US Office of Naval Research under Grant No. N00014-17-1-2283. Work at the Molecular Foundry was supported by the Office of Science, Office of Basic Energy Sciences, of the U.S. Department of Energy under Contract No. DE-AC02-05CH11231.

Data availability

The data that supports the findings of this study are available from the corresponding author upon reasonable request.

Supplementary materials

Supplementary material associated with this article can be found, in the online version, at doi:10.1016/j.actamat.2021.117461.

References

[1] E.S. Machlin, Applied voltage and the plastic properties of "brittle" rock salt, J. Appl. Phys. 30 (7) (1959) 1109–1110.
[2] W.A. Salandro, J.J. Jones, C. Bunget, J.T. Roth, L. Mears, in: Electrically Assisted Forming, Springer, 2015, pp. 23–36.
[3] K.M. Klimov, I.I. Novikov, The "electroplastic effect, Strength Mater. 16 (2) (1984) 270–276.
[4] H. Conrad, Electroplasticity in metals and ceramics, Mater. Sci. Eng. A 287 (2) (2000) 276–287.
[5] J. Andrawes, T. Kronenberger, T. Perkins, J. Roth, R. Warley, Effects of DC current on the mechanical behavior of AlMg1SiCu, Adv. Manuf. Processes 22 (1) (2007) 91–101.
[6] S. Zhao, R. Zhang, X. Li, Y. Chong, A.M. Minor, Defect reconfiguration in a Ti–Al alloy via electroplasticity, Nat. Mater. 20 (4) (2021) 468–472.
[7] X. Zhang, H. Li, M. Zhan, Z. Zheng, J. Gao, G. Shao, Electron force-induced dislocations annihilation and regeneration of a superalloy through electrical in-situ transmission electron microscopy observations, J. Mater. Sci. Technol. 36 (2020) 79–83.
[8] A.F. Sprecher, S.L. Mannan, H. Conrad, Overview no. 49: on the mechanisms for the electroplastic effect in metals, Acta Metall. 34 (7) (1986) 1145–1162.
[9] T.A. Perkins, T.J. Kronenberger, J.T. Roth, Metallic forging using electrical flow as an alternative to warm/hot working, J. Manuf. Sci. Eng. 129 (1) (2007) 84–94.
[10] A.M. Minor, G. Dehm, Advances in *in situ* nanomechanical testing, MRS Bull. 44 (6) (2019) 438–442.
[11] Q. Yu, M. Legros, A.M. Minor, In situ TEM nanomechanics, MRS Bull. 40 (01) (2015) 62–70.
[12] H. Guo, K. Chen, Y. Oh, K. Wang, C. Dejoie, S.A. Syed Asif, O.L. Warren, Z. Shan, J. Wu, A.M. Minor, Mechanics and dynamics of the strain-induced M1–M2 structural phase transition in individual VO2 nanowires, Nano Lett. 11 (8) (2011) 3207–3213.
[13] C. Chisholm, H. Bei, M. Lowry, J. Oh, S.S. Asif, O. Warren, Z. Shan, E.P. George, A.M. Minor, Dislocation starvation and exhaustion hardening in Mo alloy nanofibers, Acta Mater. 60 (5) (2012) 2258–2264.
[14] S. Vahid, G. Riccardo, D. Benoit, P. Thomas, S. Dominique, I. Hosni, Dislocation driven nanosample plasticity: new insights from quantitative in-situ TEM tensile testing, Sci. Rep. 8 (1) (2018) 12012.
[15] X. Li, A.M. Minor, Precise measurement of activation parameters for individual dislocation nucleation during *in situ* TEM tensile testing of single crystal nickel, Scr. Mater. 197 (2021) 113764.
[16] S. Kaps, S. Bhowmick, J. Gröttrup, V. Hrkac, Y.K. Mishra, Piezoresistive response of quasi-one-dimensional ZnO nanowires using an in situ electromechanical device, ACS Omega 2 (6) (2017) 2985–2993.
[17] L. Zeng, C. Gammer, B. Ozdol, T. Nordqvist, E. Olsson, Correlation between Electrical Transport and Nanoscale Strain in InAs/In0.6Ga0.4As Core-Shell Nanowires, Nano Lett. 18 (8) (2018) 4949–4956.
[18] D. Hull, D.J. Bacon, Introduction to Dislocations (Fifth Edition), Butterworth-Heinemann, 2011.
[19] Z. Wang, Q. Li, Y. Cui, Z. Liu, E. Ma, J. Li, J. Sun, Z. Zhuang, M. Dao, Z. Shan, Cyclic deformation leads to defect healing and strengthening of small-volume metal crystals, Proc. Natl. Acad. Sci. 112 (44) (2015) 13502–13507.
[20] T. Zhu, J. Li, A. Samanta, A. Leach, K. Gall, Temperature and strain-rate dependence of surface dislocation nucleation, Phys. Rev. Lett. 100 (2) (2008) 025502.
[21] C. Beaton, G. Hewitt, Physical Property Data For the Design engineer, Corp, New York, 1989.
[22] C. Ya, A. Ghajar, H. Ma, Heat and Mass Transfer Fundamentals & Applications, McGraw-Hill, 2015.
[23] F. Léonard, Reduced Joule heating in nanowires, Appl. Phys. Lett. 98 (10) (2011) 103101.
[24] W. Kang, I. Beniam, S.M. Qidwai, In situ electron microscopy studies of electromechanical behavior in metals at the nanoscale using a novel microdevice-based system, Rev. Sci. Instrum. 87 (9) (2016) 095001.
[25] Y. Touloukian, E. Buyco, Thermophysical properties of matter-The TPRC data series. Volume 5, Specific Heat-Nonmetallic solids, Thermophysical and Electronic Properties Information Analysis Center, 1970.
[26] R.F. Egerton, Control of Radiation Damage in the TEM, Ultramicroscopy, 2013.
[27] J. Dekker, A. Lodder, Calculated electromigration wind force in face-centered-cubic and body-centered-cubic metals, J. Appl. Phys. 84 (4) (1998) 1958–1962.
[28] N. Shimoni, M. Wolovelsky, O. Biham, O. Millo, Surface electromigration and self-diffusion on gold films studied via scanning tunneling microscopy, Surf. Sci. 380 (1) (1997) 100–104.
[29] O. Bondarchuk, W.G. Cullen, M. Degawa, E.D. Williams, T. Bole, P.J. Rous, Biased surface fluctuations due to current stress, Phys. Rev. Lett. 99 (20) (2007) 206801.
[30] S. To, Z. YH, L. WB, L. XM, J. YB, Effects of current density on elongation of an electropulsing treated Zn-Al based alloy, Mater. Trans. 50 (12) (2009) 2772–2777.